IEEE Access
Multidisciplinary | Rapid Review | Open Access Journal

Received April 9, 2019, accepted April 27, 2019, date of publication May 29, 2019, date of current version June 11, 2019.

Digital Object Identifier 10.1109/ACCESS.2019.2919790

A 3D Non-Stationary Wideband GBSM for Low-Altitude UAV-to-Ground V2V MIMO Channels

HENGTAI CHANG[1], JI BIAN[1], CHENG-XIANG WANG[2,3], (Fellow, IEEE), ZHIQUAN BAI[1], (Member, IEEE), WENQI ZHOU[4], AND EL-HADI M. AGGOUNE[5], (Senior Member, IEEE)

[1]Shandong Provincial Key Lab of Wireless Communication Technologies, School of Information Science and Engineering, Shandong University, Qingdao 266237, China
[2]National Mobile Communications Research Laboratory, School of Information Science and Engineering, Southeast University, Nanjing 210096, China
[3]Purple Mountain Laboratories, Nanjing 211111, China
[4]Shandong Huahan Electronics Co., Ltd., Jinan 266001, China
[5]Sensor Networks and Cellular Systems Research Center, University of Tabuk, Tabuk 47315/4031, Saudi Arabia

Corresponding author: Cheng-Xiang Wang (chxwang@seu.edu.cn)

This work was supported in part by the Fundamental Research Funds for the Central Universities under Grant 2242019R30001, in part by the Taishan Scholar Program of Shandong Province, in part by the EU H2020 RISE TESTBED Project under Grant 734325, in part by the National Science Foundation of China under Grant 61771291, in part by the Key Research and Development Plan of Shandong Province under Grant 2018GGX101009, and in part by the Sensor Networks and Cellular Systems (SNCS) Research Center, University of Tabuk.

ABSTRACT Due to the high-mobility of unmanned aerial vehicles (UAVs), actual UAV channel measurements show that low-altitude air-to-ground (A2G) channels in UAV communications illustrate non-stationary properties. This fact motivates us to develop a non-stationary channel model for UAV-to-ground links. In this paper, we propose a three-dimensional (3D) wideband non-stationary A2G vehicle-to-vehicle (V2V) geometry-based stochastic channel model (GBSM). In the proposed model, both UAVs and ground terminals can be moving, which makes the model more general. In order to mimic the non-stationary channel characteristics, parameters like the number of clusters, power, time delays, angels of departure (AoDs), and angles of arrival (AoAs) are all time-variant. The proposed model combining a line-of-sight (LoS) component, a ground reflection component, a cylinder model, and multiple confocal truncated ellipsoid models has the ability to investigate the impact of UAV heights and transceivers' movements on channel characteristics in diverse environments. Statistical properties like temporal autocorrelation function (ACF), spatial cross-correlation function (CCF), Doppler power spectral density (PSD), and stationary interval of A2G channels are derived and analyzed in detail. In addition, derived root mean square delay spread (RMS-DS), temporal ACF and spatial CCF are validated against channel measurement results. Furthermore, by adjusting channel parameters, the proposed GBSM is sufficiently generic and adaptable to model various UAV-to-ground communication scenarios.

INDEX TERMS Unmanned aerial vehicles, UAV-to-ground V2V MIMO channel models, non-stationary channel models, GBSM, statistical properties.

I. INTRODUCTION

Recently, the rapid development of unmanned aerial vehicle (UAV) industry calls for the need of high-speed and reliable UAV communication technologies [1]. To meet this urgent need, many organizations and companies implemented research and development projects such as the ''Loon'' [2] by Google and the ''enhanced long time evolution (LTE) support for aerial vehicles'' [3] by the 3rd Generation Partnership Project (3GPP). AT&T and Qualcomm also did optimization for LTE on UAV communications [4]. In the forthcoming fifth generation (5G) and beyond 5G (B5G) wireless communication networks, UAV communications would become an important application scenario due to the high-reliable need for control and non-payload communications (CNPCs) [5]. Besides, UAVs are appealing to serve as platforms of air base

The associate editor coordinating the review of this manuscript and approving it for publication was Ke Guan.

stations (BSs) or airborne relays which can be favourable complement of terrestrial BSs and further extend wireless network coverage as they can be dispatched quickly, flexibly, and with low-cost [6].

Many previous investigations revealed that channel models are indispensable for wireless communication system design and performance evaluation. However, compared with other high mobility communication scenarios such as vehicle-to-vehicle (V2V) [7]–[9] and high-speed train [10]–[14] (HST) scenarios, the current UAV communication channel investigation is still insufficient. Since current commercial UAVs usually stay at lower altitudes than manned crafts, in order to provide reliable UAV-to-ground communication links, the knowledge of underlying low-altitude air-to-ground (A2G) propagation channels is required. Compared with terrestrial wireless communication channels, UAV-to-ground channels present a number of distinct properties. In UAV-to-ground communications, the transmitters (Tx) mounted on the UAV can move in three-dimensional (3D) environments which means that the A2G channel models have to take into account the 3D communication environment space. Besides, UAVs and ground terminals can stay at different altitudes. Therefore, in A2G channel modeling, the impacts of A2G elevation angels and altitudes of the UAVs should be introduced and investigated. Meanwhile, the characteristics of the A2G channel depend on the communication environments to a great extent. For the A2G channels in open field scenarios such as suburban and over-water, the line-of-sight (LoS) component contributes mostly to the received power. But for the low-altitude A2G channels in complex environments like urban and hilly scenario, the multi-path propagations will have great impacts on the channel properties. In addition, the fast-moving Tx and/or receiver (Rx) makes the channel non-stationary in the time domain [16], which causes the wide-sense-stationary (WSS) assumption to be invalid. Consequently, the non-stationary channel modeling should be taken into account to capture the fast-variant UAV channel characteristics.

In the literature, existing A2G channel models can be divided into deterministic channel models and stochastic channel models. In [21], a deterministic A2G channel model for urban environments based on the ray-tracing method was proposed. In [22], the air-to-air (A2A) channels between UAVs and vessels were investigated using the finite-difference-time-domain (FDTD) method. As typical deterministic channel modeling methods, ray-tracing and FDTD methods are adequate accurate for certain communication scenarios with known environment parameters but not sufficiently flexible to describe the general and unknown environments parameters UAV communication channels. Therefore, the practicability of deterministic channel modeling methods is limited. On the contrary, the geometry-based stochastic channel model (GBSM) method is a typical stochastic channel modeling method that has been widely used to simulate wireless channels due to its good balance between accuracy, complexity, and easy to use. In [24]–[26], GBSMs for UAV-to-ground scenarios utilizing the single cylinder geometry model were proposed to describe the A2G channel environments and some channel characteristics such as spatial correlation function and temporal correlation function were analyzed. However, the existing UAV GBSMs are mostly based on the narrowband assumption, wherein different multipath components have same time delays which dose not confirm the exact A2G channels. In [27] and [28], angels of arrival (AoAs) for A2G channels were derived based on a wideband slant ellipsoid geometry channel model. However, the mobilities of both UAVs and ground terminals were neglected and the studied parameters are limited to AoAs and channel capacities, which are not exhaustive enough to reveal the UAV-to-ground channel properties. Another wideband A2G channel model [29] took into account the impacts of tranceivers movements and but the fact that scatterers can not appear in high altitude and underground was neglected.

In [30], we proposed a wideband GBSM for low-altitude UAV-to-ground channels. Our previous proposed model and most current A2G channel models are based on WSS assumption. However, in [17]–[19], a series of measurement campaigns were conducted and measurement results verified that A2G channel statistics will change over time while the UAV and ground terminal are moving. Therefore, mobile UAV-to-ground channels present obvious non-stationary properties. According to the measurement results, WSS assumption is only valid for short time periods. Hence, the non-stationary aspects of A2G channels in channel modeling must be carefully taken into account.

In this paper, we propose a novel 3D wideband non-stationary V2V GBSM to describe the low altitude non-stationary A2G channels. The proposed GBSM contains a LoS component, a ground reflection component, a single cylinder model, and multiple confocal truncated ellipsoid models with single bounce (SB) and double bounced (DB) rays. Moreover, the markov birth-death process and time-variant cluster parameters are applied to model the channel changing over time. The model is sufficiently generic and adaptable to model various non-stationary UAV-to-ground communication scenarios. In addition, in UAV-to-ground communication scenarios, scatterers like buildings and terrains cannot be distributed in the air or underground. Thus, in order to increase the accuracy, in our model, scatterer altitudes are restricted to a certain range. Based on the proposed model, we derive and analyze some important channel characteristics including temporal autocorrelation function (ACF), spatial cross-correlation function (CCF), Doppler power spectral density (PSD), time-variant transfer function, root mean square delay spread (RMS-DS), and stationary interval. Finally, in order to increase the practicability and reduce the computation complexity, the corresponding sum of sinusoids (SoS) simulation model is developed.

Overall, the main contributions and innovations of this paper are summarized as below:

1) Based on our previous work in [30], the extension for non-stationary V2V GBSM is proposed with time-varying parameters. The proposed A2G V2V channel model considers the impacts of different UAV altitudes and A2G elevation angles on scattering region.
2) In order to mimic non-stationary behavior caused by moving UAVs and ground terminals, we introduce the birth-death process and smooth transition region to model the cluster evolution.
3) Important channel statistical properties, such as space-time correlation function (STCF), Doppler PSD, RMS-DS, and stationary interval, are derived and thoroughly investigated.
4) The proposed non-stationary V2V GBSM is validated by comparing the statistical properties with measurement results in different scenarios. Therefore our model can be adopted to diverse UAV-to-ground communication scenarios by adjusting model parameters.

The rest of this paper is organized as follows. In Section II, the 3D wideband non-stationary GBSM is described. The propagation environment, geometry relationship, cluster birth-death, and evolution process are presented in detail. In Section III, some significant channel characteristics such as STCF, Doppler PSD, transfer function, RMS-DS, and stationary interval are derived based on the proposed model. Section IV develops the corresponding SoS simulation model and presents the channel simulation results and analysis. Section V concludes the whole investigation works and gives several future research directions.

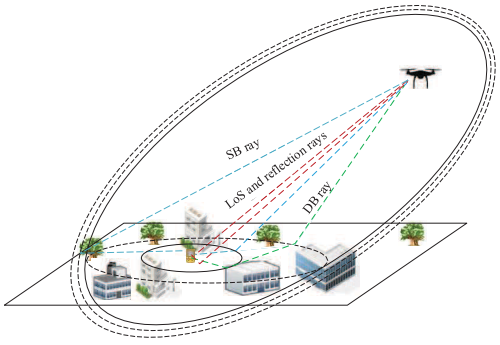

FIGURE 1. A typical UAV-to-ground communication scenario with all possible channel components including LoS, ground reflection, SB scattering components, and DB scattering components.

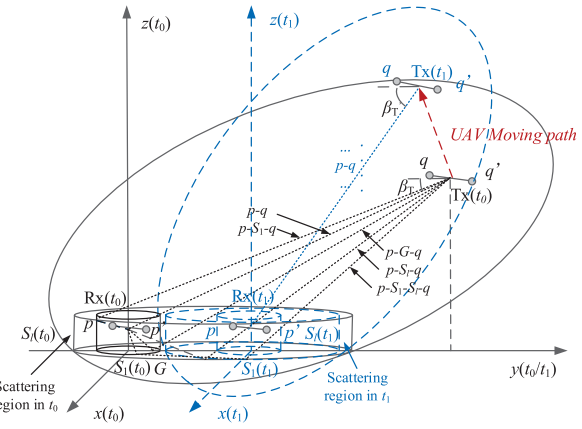

FIGURE 2. The proposed 3D non-stationary GBSM for UAV-MIMO channels ($M_T = M_R = 2$).

II. 3D WIDEBAND A2G V2V MIMO GBSM

In order to make proposed channel model more general, all possible channel components are included in our model. According to available A2G channel measurements [17], [19], LoS and ground reflection components play important roles in open field while scattering components have more contribution in complex environments. In Fig. 1, the general description of proposed GBSM including a LoS component, a ground reflection component, and SB/DB scattering components result from nearby and distant scatterers is presented. Note that the scatterer movements usually have negligible impacts on A2G channels according to previous investigation [36]. Thus, in our proposed model, only static scatterers are considered.

A detailed 3D non-stationary MIMO channel between the UAV with M_T omni-directional antenna elements and the ground terminal with M_R omni-directional antenna elements is shown in Fig. 2. The UAV-to-ground V2V MIMO fading channel can be represented by a matrix $H(t) = [h_{pq}(t,\tau)]_{M_R \times M_T}$, $(p = 1, \ldots, M_R, q = 1, \ldots, M_T)$ of size $M_R \times M_T$. Since UAVs usually carry out complex operations such as rising, diving, and hovering, the moving direction of UAV have to be described by both azimuth and elevation angles. Here γ_T and ξ_T are azimuth and elevation angels of the UAV moving direction, respectively. As for the ground terminal, since the ground terminals only can move on the ground plane, the velocity direction can be simply described by single azimuth angle γ_R. To simplify the latter calculation, velocity vectors of Tx and Rx having expression $\mathbf{v}_T = v_T[\cos\gamma_T \cos\xi_T \ \ \sin\gamma_T \cos\xi_T \ \ \sin\xi_T]$ and $\mathbf{v}_R = v_R[\cos\gamma_R \ \ \sin\gamma_R \ 0]$ are introduced, where v_T and v_R are velocities of the UAV and ground terminal.

In Fig. 2, G denotes the ground reflection point on the ground plane. The cylinder around the Rx denotes nearby scattering region around Rx and containing N_1 scattering rays. The multiple confocal ellipsoids taking transceivers as focal points denote the distant scattering structure and have N_l effective scattering rays on the l-th ellipsoid, where $l = 2, 3, \ldots, L(t)$ and $L(t)$ is the total scatterers number at time t. Considering that scatterers rarely appear in the air or underground, we limited the scattering region to the space on and near the ground plane. Specifically, the distant scattering region on the ground is the cross sections of multi-confocal ellipsoids and the ground plane. Since that intersecting surface of a ellipsoid is a ellipse, we can use an expression of the ellipse to represent the scattering region on the ground plane. Then, as that scatterers such as buildings and trees generally have vertical straight structure relative to ground plan, the elliptical cylinder model could be constructed based

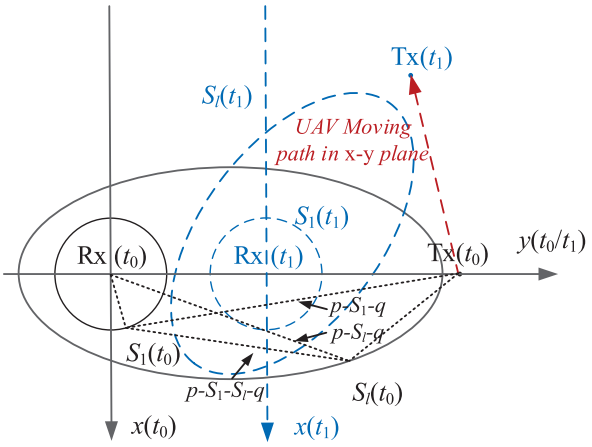

FIGURE 3. The proposed 3D non-stationary GBSM for UAV-MIMO channels projected in x-y plane.

on the truncated ellipse to represent scattering region in the 3D environment based on the elliptical truncated surface. To facilitate readers' understanding, Fig. 3 gives the planar graph of Fig. 2, and the MIMO structure is removed to reduce complexity.

A. EFFECTIVE SCATTERING REGION

Considering the movements of the UAV and ground terminal, the location of Tx and Rx are time-variant. In order to simplify the follow-up calculation, we set the projection of ground terminal on ground plane as the origin of coordinate, and use $\mathbf{L}_T(t)$ and $\mathbf{L}_R(t)$ to represent the 3D locations of Tx and Rx. Meanwhile, we use $\mathbf{S}_1(t)$ to represent the center location of nearby scatterers distributed on the cylinder and use $\mathbf{S}_l(t)$, $(l > 1)$ to represent the center location of scatterer distributed on the truncated ellipsoids. In Fig. 2, due to the movements of UVA and ground terminal, the distant scattering region number as l changes from the black solid part to the blue dashed part. Therefore, the scattering region should be calculated at different time instants.

In order to obtain the formula expression of time-variant truncated elliptical scattering region on the ground plane, we substitute expression of ground plane into ellipsoid to get number l elliptical expression of truncated ellipsoid which has time delay τ_l as

$$Ax^2 + By^2 + Cxy + Dx + Ey + F = 0. \tag{1}$$

The definition of A–F and detailed geometry derivation can be find in Appendix and no more repetition here.

B. CHANNEL IMPULSE RESPONSE

According to the time delay line (TDL) concept, the complex channel impulse response (CIR) of MIMO fading channel between the p-th Rx antenna element and q-th Tx antenna element can be represented by

$$h_{pq}(t,\tau) = \sum_{l=1}^{L(t)} \sqrt{P_l(t)} h_{l,pq}(t)\delta(\tau - \tau_l) \tag{2}$$

in which $P_l(t)$ denotes the time-variant power of the l-th tap, $h_{l,pq}(t)$ is the l-th tap's complex coefficient, and τ_l denotes the time delay of the l-th tap.

In the above CIR expression, the whole CIR is the superposition of several taps having different propagation delays and power, and channel components in the same tap have the same time delays. For the first tap, obviously, the LoS component having the shortest propagation distance and the minimum time delay is included. In addition, since the ground terminal in our model stay at low altitudes, the ground reflection component has similar propagation distance and time delay. At last, the radius of nearby cylinder scattering region is much smaller than the distance between Tx and Rx, i.e., $R \ll D_{\mathrm{LoS}}$, so SB scattering rays on nearby cylinder model can also be included in the first tap. Therefore, the complex coefficient of first tap have the following expression

$$h_{1,pq}(t) = h_{pq}^{\mathrm{LoS}}(t) + h_{pq}^{\mathrm{Ref}}(t) + h_{pq}^{\mathrm{SB}_1}(t) \tag{3}$$

with

$$h_{pq}^{\mathrm{LoS}}(t) = \sqrt{\frac{K}{K+1}} e^{jk_0(\mathbf{r}_p\cdot\Phi_{\mathrm{LoS}}(t)+\mathbf{r}_q\cdot\Psi_{\mathrm{LoS}}(t))} \times e^{j2\pi f_{\mathrm{Tm}}(\mathbf{v}_T\cdot\Phi_{\mathrm{LoS}}(t))}\cdot e^{j2\pi f_{\mathrm{Rm}}(\mathbf{v}_R\cdot\Psi_{\mathrm{LoS}}(t))} \tag{4}$$

$$h_{pq}^{\mathrm{Ref}}(t) = \sqrt{\frac{\eta_r}{K+1}} e^{jk_0(\mathbf{r}_p\cdot\Phi_{\mathrm{LoS}}(t)+\mathbf{r}_q\cdot\Psi_{\mathrm{Ref}}(t)+\theta_r)} \times e^{j2\pi f_{\mathrm{Tm}}(\mathbf{v}_T\cdot\Phi_{\mathrm{Ref}}(t))}\cdot e^{j2\pi f_{\mathrm{Rm}}(\mathbf{v}_R\cdot\Psi_{\mathrm{Ref}}(t))} \tag{5}$$

$$h_{pq}^{\mathrm{SB}_1}(t) = \sqrt{\frac{\eta_{\mathrm{SB}_{1,n}}}{K+1}} \lim_{N_1\to\infty}\sum_{n=1}^{N_l}\frac{1}{\sqrt{N_l}} \times e^{jk_0(\mathbf{r}_p\cdot\Phi_{\mathrm{SB}_{1,n}}(t)+\mathbf{r}_q\cdot\Psi_{\mathrm{SB}_{1,n}}(t)+\theta_{1,n})} \times e^{j2\pi f_{\mathrm{Tm}}(\mathbf{v}_T\cdot\Phi_{\mathrm{SB}_{1,n}}(t))}\cdot e^{j2\pi f_{\mathrm{Rm}}(\mathbf{v}_R\cdot\Psi_{\mathrm{SB}_{1,n}}(t))} \tag{6}$$

where K is the Rician factor, η_r and $\eta_{\mathrm{SB},1}$ specify how much the ground reflection and SB rays contribute to the total power of the first tap. Note that these energy-related parameters are normalized to satisfy $\eta_r + \eta_{\mathrm{SB},1} = 1$.

The complex tap coefficient for other taps $(l > 1)$ of the UAV-to-ground link is a superposition of the SB and DB scattering components, and can be expressed as

$$h_{l,pq}(t) = h_{pq}^{\mathrm{SB}_l}(t) + h_{pq}^{\mathrm{DB}_l}(t) \tag{7}$$

with

$$h_{pq}^{\mathrm{SB}_l}(t) = \sqrt{\eta_{\mathrm{SB}_l}} \lim_{N_l\to\infty}\sum_{n=1}^{N_l}\frac{1}{\sqrt{N_l}} \times e^{jk_0(\mathbf{r}_p\cdot\Phi_{\mathrm{SB}_{l,n}}(t)+\mathbf{r}_q\cdot\Psi_{\mathrm{SB}_{l,n}}(t)+\theta_{l,n})} e^{j2\pi f_{\mathrm{Tm}}(\mathbf{v}_T\cdot\Phi_{\mathrm{SB}_{l,n}}(t))} \cdot e^{j2\pi f_{\mathrm{Rm}}(\mathbf{v}_R\cdot\Psi_{\mathrm{SB}_{l,n}}(t))} \tag{8}$$

$$h_{pq}^{\mathrm{DB}_l}(t) = \sqrt{\eta_{\mathrm{DB}_l}} \lim_{N_1,N_l\to\infty}\sum_{n=1}^{N_1 N_l}\frac{1}{\sqrt{N_1 N_l}} \times e^{jk_0(\mathbf{r}_p\cdot\Phi_{\mathrm{DB}_l}(t)+\mathbf{r}_q\cdot\Psi_{\mathrm{DB}_l}(t)+\theta_{l,n})} e^{j2\pi f_{\mathrm{Tm}}(\mathbf{v}_T\cdot\Phi_{\mathrm{DB}_l}(t))} \cdot e^{j2\pi f_{\mathrm{Rm}}(\mathbf{v}_R\cdot\Psi_{\mathrm{DB}_l}(t))} \tag{9}$$

where $\eta_{\mathrm{SB},l}$ and $\eta_{\mathrm{DB},l}$ specify how much the SB and DB rays contribute to the total scattered power of the l-th tap.

Also energy-related parameters are normalized to satisfy $\eta_{\mathrm{SB},l} + \eta_{\mathrm{DB},l} = 1$. The coordinates of antenna element p at Tx side and antenna element q at Rx side, i.e., $\mathbf{r}_p$ and $\mathbf{r}_q$, are local coordinate systems (LCSs) relative to the center of the Tx antenna array and Rx antenna array, respectively. In our proposed analytical channel model, the number of rays in each cluster is assumed to be infinity. In (4)–(9), vectors represented by $\Phi(t)$ and $\Psi(t)$ denote the time-variant arrival and departure angle unit vectors of the different rays in different clusters respectively. For example, angel of arrival (AoA) and angel of departure (AoD) of n-th ray in l-th cluster can be expressed as $\Psi_{\mathrm{SB}_{l,n}}(t) = [\cos\alpha_R^{\mathrm{SB}_{l,n}} \cos\beta_R^{\mathrm{SB}_{l,n}} \quad \sin\alpha_R^{\mathrm{SB}_{l,n}} \cos\beta_R^{\mathrm{SB}_{l,n}} \quad \sin\beta_R^{\mathrm{SB}_{l,n}}]$ and $\Phi_{\mathrm{SB}_{l,n}}(t) = [\cos\alpha_T^{\mathrm{SB}_{l,n}} \cos\beta_T^{\mathrm{SB}_{l,n}} \quad \sin\alpha_T^{\mathrm{SB}_{l,n}} \cos\beta_T^{\mathrm{SB}_{l,n}} \quad \sin\beta_T^{\mathrm{SB}_{l,n}}]$, where $\alpha_{\mathrm{T/R}}^{\mathrm{SB}_{l,n}}$ and $\beta_{\mathrm{T/R}}^{\mathrm{SB}_{l,n}}$ denote azimuth and elevation angle of departure/arrival of n-th ray in l-th cluster. In this paper, we use von-Mises distribution, which is widely used in wireless channel modelling, to describe azimuth AoA (AAoA). In term of the elevation angle, since the height of scatters is limited, cosine distribution which has upper limit and lower limit is used to describe elevation AoA (EAoA) [24]. The von-Mises distribution can be expressed as

$$f(\alpha) = \frac{e^{k\cos(\alpha-\alpha_\mu)}}{2\pi I_0(k)}, \quad 0 < \alpha \le 2\pi \tag{10}$$

where $I_0(\cdot)$ denotes the first kind zero-order modified Bessel function, $\alpha_\mu \in (0, 2\pi]$ denotes the mean angle that the AAoAs are mainly distributed, and parameter k gives a measure of the angel spread around the mean angle α_μ. The cosine distribution describing the EAoAs can be expressed

$$f(\beta) = \frac{\pi}{4\beta_\mu}\cos(\frac{\pi}{2}\frac{\beta-\beta_\mu}{\beta_m}), \quad \beta_\mu - \beta_m < \beta \le \beta_\mu + \beta_m \tag{11}$$

where β_μ is the mean direction of EAoA and β_m is the variance of β. The upper limit and lower limit of cosine distribution are $\beta_u + \beta_m$ and $\beta_u - \beta_m$ respectively. According to the definition of scatterer center, the AAoA and EAoA of scatterer center is α_μ and β_μ respectively.

In addition, $k_0 = 2\pi/\lambda$ denotes the wavenumber, in which λ is the wavelength of the carrier. The random phase shift θ_r and $\theta_{l,n}$ caused by reflection and scattering respectively are independent identically distributed (i.i.d.) random variables and they are uniformly distributed in $(0, 2\pi]$. Other related parameters are listed and described in Table 1.

C. CLUSTER EVOLUTION PROCESS

Considering the movements of UAVs and ground terminals, the cluster not existing in the last time instant may appear in next time instant. Meanwhile, a cluster may exist for a time period and disappear in the next time instant. Thus, it is feasible to develop a non-stationary channel model based on our GBSM by imposing the cluster birth-death process.

In the proposed non-stationary GBSM, as time goes on, clusters appear, exist for certain time periods, and finally disappear. A appropriate description for such a generation and recombination phenomenon can be provided by the discrete Markov process. The time variation of UAV-to-ground channels is mainly caused by movements of UAVs and ground terminals. Therefore, a variable "movement of scenarios" is introduced to evaluate the variation of A2G wireless channels in the time period from t to $t + \Delta t$, and it can be described as

$$\delta_P(t, \Delta t) = \delta_R(t, \Delta t) + \delta_T(t, \Delta t) \tag{12}$$

where $\delta_R(t, \Delta t)$ and $\delta_T(t, \Delta t)$ are channel variation caused by Rx and Tx respectively and can be defined as

$$\delta_R(t, \Delta t) = \int_t^{t+\Delta t} v_R(t)\, dt \tag{13}$$

$$\delta_T(t, \Delta t) = \int_t^{t+\Delta t} v_T(t)\, dt. \tag{14}$$

Because of the short time interval, we assume that the UAV and ground terminal move with a constant speed in time interval Δt and the equation can be simplified to

$$\delta_R(t, \Delta t) = v_R(t)\Delta t \tag{15}$$

$$\delta_T(t, \Delta t) = v_T(t)\Delta t. \tag{16}$$

Therefore, $\delta_P(t, \Delta t)$ provides the correlation extent of CIRs between different time instants. Introduced Markov birth-death process described in [16] leads to the time-variant number of clusters, $L(t)$, for CIR generation realizations. At a certain time instant t, newly generated clusters and clusters already existing in the previous CIR at time instant $t - \Delta t$ can be processed separately. The Markov process is described by a generation rate of clusters (λ_G) and a recombination rate of clusters (λ_R). The expectation of the total distant scatterer number, also defined as the initial distant scatterer number, can be obtained by

$$\mathbf{E}[L(t)] = \frac{\lambda_G}{\lambda_R}. \tag{17}$$

TABLE 1. Definition of significant parameters.

Symbol	Definition
$D_{\mathrm{LoS}}(t)$	Distance between Tx and Rx
φ	Elevation angle of LoS path
R	Radius of cylinder scattering region
S_l	3D position of l-th scatterer
$\Delta d_R(\Delta d_T)$	Antenna element spacing at Rx (Tx)
$\alpha_R(\alpha_T)$	Azimuth angle of Rx (Tx) orientation
$\beta_R(\beta_T)$	Elevation angle of Rx (Tx) orientation
$h_1(h_2)$	Altitude of Rx (Tx)
$f_{\mathrm{Rm}}(f_{\mathrm{Tm}})$	Maximum Doppler frequency at Rx (Tx)
$\alpha_R^{\mathrm{LoS}}(\beta_R^{\mathrm{LoS}})$	AAoA/EAoA of LoS component
$\alpha_T^{\mathrm{LoS}}(\beta_T^{\mathrm{LoS}})$	AAoD/EAoD of LoS component
$\alpha_R^{\mathrm{Ref}}(\beta_R^{\mathrm{Ref}})$	AAoA/EAoA of reflection component
$\alpha_T^{\mathrm{Ref}}(\beta_T^{\mathrm{Ref}})$	AAoD/EAoD of reflection component
$\mathbf{v}_T$	Tx velocity vector
$\mathbf{v}_R$	Rx velocity vector

Meanwhile, the probabilities of cluster survive from t to $t+\Delta t$ can be expressed as

$$P_{\text{surv}}(\Delta t) = e^{-\lambda_R \frac{\delta_P(t,\Delta t)}{D_c}} \tag{18}$$

where D_c is the correlation factor depend on the scenario. At last, the number of new clusters that is generated by the Markov process in time period t to $t+\Delta t$ have the expectation of

$$\mathbf{E}[L_{\text{New}}(\Delta t)] = \frac{\lambda_G}{\lambda_R}(1 - e^{-\lambda_R \frac{\delta_P(t,\Delta t)}{D_c}}). \tag{19}$$

For the generation process of the new cluster, the time delay is firstly defined by $\tau_l = \tau_{\text{LoS}}(t) + \widetilde{\tau}_l$, where $\widetilde{\tau}_l$ is virtual delays of generated cluster which assumed to be exponentially distributed, and can be realized by

$$\widetilde{\tau}_l = -r_\tau \sigma \cdot \ln u_l \tag{20}$$

where r_τ, σ denote the delay scalar and delay spread respectively, and u_n follows the uniform distribution in (0,1). Besides, $\tau_{\text{LoS}}(t)$ denotes the time-variant time delay of LoS path which can be expressed by

$$\tau_{\text{LoS}}(t) = D_{\text{LoS}}(t)/c \tag{21}$$

$$D_{\text{LoS}}(t) = \parallel \mathbf{L}_T(t) - \mathbf{L}_R(t) \parallel \tag{22}$$

where $\mathbf{L}_T(t)$, $\mathbf{L}_R(t)$ are the locations of the UAV and ground terminal which can be calculated as

$$\mathbf{L}_T(t) = \mathbf{L}_T(t-\Delta t) + \mathbf{v}_T \Delta t - \mathbf{v}_R \Delta t \tag{23}$$

$$\mathbf{L}_R(t) = \mathbf{L}_R(t-\Delta t). \tag{24}$$

Then scattering region can be calculated according to (1). The x, y, and z components of new generated $\mathbf{S}_{l,n}$, i.e., $x_{l,n}$, $y_{l,n}$, and $z_{l,n}$ have the expressions as

$$\begin{aligned} x_{l,n} &= -\frac{F' \tan \alpha_R^{\text{SB}_{l,n}} + D \tan \alpha_R^{\text{SB}_{l,n}} + E \tan^2 \alpha_R^{\text{SB}_{l,n}}}{2 \tan \alpha_R^{\text{SB}_{l,n}} (B \tan^2 \alpha_R^{\text{SB}_{l,n}} + C \tan \alpha_R^{\text{SB}_{l,n}} + A)} \\ y_{l,n} &= x_{l,n} \tan \alpha_R^{\text{SB}_{l,n}} \\ z_{l,n} &= \sqrt{{x_{l,n}}^2 + {y_{l,n}}^2} \tan \beta_R^{\text{SB}_{l,n}}, \quad l > 1 \end{aligned} \tag{25}$$

where $F' = (D^2 + 2DE \tan^2 \alpha_R^{\text{SB}_{l,n}} + E \tan^2 \alpha_R^{\text{SB}_{l,n}} - 4BF \tan^2 \alpha_R^{\text{SB}_{l,n}} - 4CF \tan \alpha_R^{\text{SB}_{l,n}} - 4AF)^{\frac{1}{2}}$, and α_R^{SB}, β_R^{SB}, α_T^{SB}, β_T^{SB} denote AAoA, EAoA, azimuth AoD (AAoD), and elevation AoD (EAoD) for different rays, respectively.

In all, at the beginning, $\mathbf{E}[L(t)]$ distant scatters and one nearby scatterer are generated according to cluster generation process. With ongoing time, at the beginning of each time period Δt, disappearing clusters are removed from CIRs and new generated clusters are added into CIRs. At the same time, due to the location changes of both Tx and Rx, parameters of surviving clusters will change in time period Δt. Hence, we applied the evolution process to model surviving clusters.

D. EVOLUTION OF SURVIVING CLUSTERS

1) Update delays: During the surviving period, the time delay of each cluster will change according to related distance between Tx, scatterers, and Rx. Since the movements of scatterers usually have negligible influence on channels, we just assume every distant scatterer has the relative movement to dynamic coordinate origin,

$$\begin{aligned} \mathbf{S}_{l,n}(t) &= \mathbf{S}_{l,n}(t-\Delta t) - \mathbf{v}_R \Delta t \\ \mathbf{S}_l(t) &= \mathbf{S}_l(t-\Delta t) - \mathbf{v}_R \Delta t, \quad l > 1. \end{aligned} \tag{26}$$

Thus, the time-variant propagation distances of different taps can be obtained by

$$D_{l,\text{T/R}}(t) = \parallel \mathbf{L}_{\text{T/R}}(t) - \mathbf{S}_l(t) \parallel, \quad l > 1 \tag{27}$$

where $D_{l,\text{T/R}}(t)$ denote the distances between the l-th scatterer and Tx (Rx). Then we can get the time delay of taps caused by distant scattering region $l > 1$

$$\tau_l(t) = (D_{l,R}(t) + D_{l,T}(t))/c \tag{28}$$

where τ_l are path delays of the l-th taps in CIR expression. As for the delay of first tap, it can represented by $\tau_1(t) \approx \tau_{\text{LoS}}(t)$.

2) Update power: The time-variant cluster power can be calculated by a single slope exponential power delay profile with the attenuation factor according to the taps' time delay $\tau_l(t)$. The cluster power can be defined according to time-variant cluster delay $\tau_l(t)$ and other parameters by

$$P_l'(t) = \left[\exp\left(-\tau_l(t)\frac{1-r_\tau}{r_\tau \sigma}\right) 10^{-\frac{Y_l}{10}}\right]$$

where Y_l follows the Gaussian distribution. Besides, when clusters fade in and fade out, the power of cluster will present a transition process. In order to realize the smooth transition behaviour, the transition region is applied while cluster appearing and disappearing [33]. Here, the power of each cluster is multiplied by the power control factor $\xi_l(t)$ defined by

$$\begin{aligned} &\xi_l(t) \\ &= -\frac{1}{\pi} \cdot \arctan\left(\frac{2[L_c + (|2t - T_l| - T_l) \cdot (v_T + v_R)]}{\sqrt{\lambda \cdot L_c}}\right) \\ &\quad + \frac{1}{2}, \quad t \in (0, T_l) \end{aligned} \tag{29}$$

in which T_l is the lifetime of the l-th cluster, and L_c is the length of the transition region. With this power control factor, the cluster birth-death process can be more smooth. Since the proposed channel model mainly investigate the small-scale fading, the total received power is normalized to one, and the normalization process can be expressed as

$$P_l(t) = \frac{|\xi_l(t)|^2 P_l'(t)}{\sum_{l=1}^{L(t)} |\xi_l(t)|^2 P_l'(t)}. \tag{30}$$

3) Update angle parameters: For the scattering rays, the position vector of the n-th scattering point in l-th scatterers $\mathbf{S}_{l,n}$ can be obtained according to (25)(31). Note that in the dynamic coordinate, distant scatterers $\mathbf{S}_l$ are moving like expressed in (27), nearby scatterer $\mathbf{S}_1$ is static like: $\mathbf{S}_1(t) = \mathbf{S}_1(t - \Delta t)$ and the x, y, and z components of $\mathbf{S}_{1,n}$, i.e., $x_{1,n}$, $y_{1,n}$, and $z_{1,n}$ have the expressions as

$$\begin{aligned} x_{1,n} &= R\cos\alpha_R^{\mathrm{SB}_{1,n}} \\ y_{1,n} &= x_{1,n}\tan\alpha_R^{\mathrm{SB}_{1,n}} \\ z_{1,n} &= \sqrt{{x_{1,n}}^2 + {y_{1,n}}^2}\tan\beta_R^{\mathrm{SB}_{1,n}}. \end{aligned} \tag{31}$$

The relationship between AoA and AoD can be obtained by geometric algorithm as

$$\beta_{\mathrm{T/R}}^{\mathrm{SB}_{l,n}} = \arcsin\frac{z_{l,n} - z_{\mathrm{T/R}}}{D_{l,\mathrm{T/R}}(t)}) \tag{32}$$

$$\alpha_{\mathrm{T/R}}^{\mathrm{SB}_{l,n}} = \begin{cases} \arctan(\dfrac{x_{l,n} - x_{\mathrm{T/R}}}{y_{l,n} - y_{\mathrm{T/R}}}), & x_{l,n} - x_{\mathrm{T/R}} > 0 \\ \arctan(\dfrac{x_{l,n} - x_{\mathrm{T/R}}}{y_{l,n} - y_{\mathrm{T/R}}}) + \pi, & x_{l,n} - x_{\mathrm{T/R}} \le 0. \end{cases} \tag{33}$$

Similarly, according to geometric algorithm, the AAoA and EAoA of DB components are equal to those of SB components on the cylinder scattering region, and AAoD and EAoD of DB components are equal to those of SB components on the l-th truncated ellipsoid scattering region. At last, in terms of LoS and ground reflection components, we can get

$$\beta_R^{\mathrm{LoS}} = \arcsin\frac{z_T - z_R}{D_{\mathrm{LoS}}(t)}) \tag{34}$$

$$\alpha_R^{\mathrm{LoS}} = \begin{cases} \arctan(\dfrac{x_T - x_R}{y_T - y_R}), & x_T - x_R > 0 \\ \arctan(\dfrac{x_T - x_R}{y_T - y_R}) + \pi, & x_T - x_R \le 0. \end{cases} \tag{35}$$

In case of AAoD, EAoD of LoS component α_T^{LoS} and β_T^{LoS}: $\alpha_T^{\mathrm{LoS}} = -\alpha_R^{\mathrm{LoS}}$, $\beta_T^{\mathrm{LoS}} = -\beta_R^{\mathrm{LoS}}$. The angle parameters of the ground reflection component are updated using the similar process: $\alpha_{\mathrm{T/R}}^{\mathrm{Ref}} = \alpha_{\mathrm{T/R}}^{\mathrm{LoS}}$, and $\beta_{\mathrm{T/R}}^{\mathrm{Ref}} = -\arctan((z_T + z_R)/\sqrt{(x_T - x_R)^2 + (y_T - y_R)^2})$.

The cluster power and time delays in LoS scenario, i.e., the power delay profile (PDP) of the proposed model, are depicted at the time instant $t = 1$s in Fig. 4. It can be observed that clusters more likely to appear at lower time delays the cluster with higher time delay tends to have lower power. Fig. 5 illustrates the cluster evolution process in non-LoS (NLoS) scenario. The expectation of cluster number is set to $\mathbf{E}[L(t)] = 20$, a smooth cluster birth-death process can be observed when clusters appear and disappear.

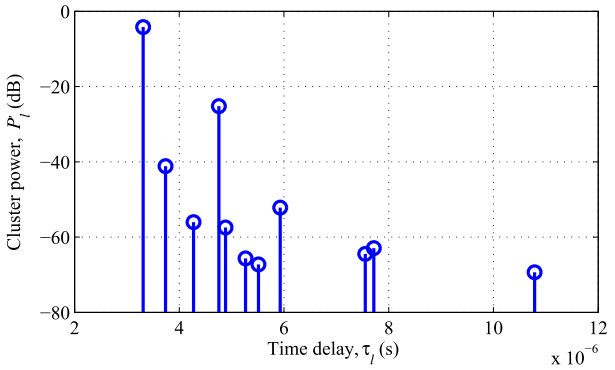

FIGURE 4. A snapshot of the cluster power and cluster time delays at $t = 1$s ($K = 10$, $\eta_r = 0.2$, $\eta_{\mathrm{SB}_1} = 0.8$, $\eta_{\mathrm{SB}_l} = 0.9$, $\eta_{\mathrm{DB}_l} = 0.1$, $\lambda_G = 0.8$, $\lambda_R = 0.08$).

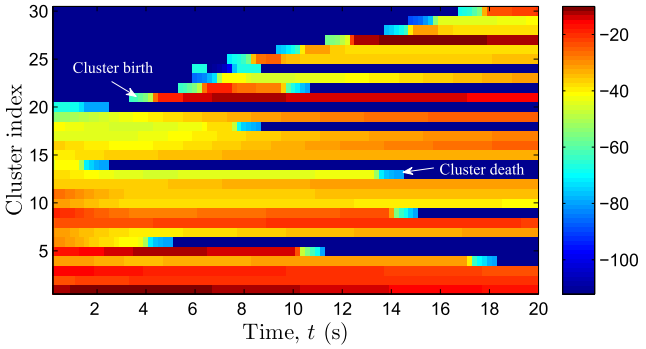

FIGURE 5. Time-variant clusters with birth death process ($L(t_0) = 20$, $\lambda_G = 0.8$, $\lambda_R = 0.04$, $v_T = 10$ m/s, $v_R = 5$ m/s, $D_c = 10$ m, $L_c = 60$ m).

III. CHANNEL CHARACTERISTICS

A. LOCAL STCF

In this paper, the normalized local complex STCF for proposed non-stationary GBSM is defined as

$$\rho_{h_{pq}h_{p'q'}}(t, \Delta t) = \frac{\mathbf{E}[h_{pq}(t)h^*_{p'q'}(t - \Delta t)]}{\sqrt{\mathbf{E}[|h_{pq}(t)|^2]\mathbf{E}[|h^*_{p'q'}(t - \Delta t)|^2]}} \tag{36}$$

where $(\cdot)^*$ is the complex conjugate operation. Since the correlation properties are completely determined by correlation properties of each tap, and no correlation existing between different clusters is assumed. The STCF can be expressed

$$\rho_{h_{pq}h_{p'q'}}(t, \Delta t) = \sum_{l=1}^{L(t)} P_l(t)\rho_{h_{l,pq}h_{l,p'q'}}(t, \Delta t). \tag{37}$$

In case of the first tap, i.e., the superposition of LoS, ground reflection, and cylinder scattering components, the STCF can be written as

$$\begin{aligned} \rho_{h_{1,pq}h_{1,p'q'}}(t, \Delta t) = {} & \rho^{\mathrm{LoS}}_{h_{1,pq}h_{1,p'q'}}(t, \Delta t) + \rho^{\mathrm{Ref}}_{h_{1,pq}h_{1,p'q'}}(t, \Delta t) \\ & + \rho^{\mathrm{SB}_1}_{h_{1,pq}h_{1,p'q'}}(t, \Delta t). \end{aligned} \tag{38}$$

Whereas for other taps, we have

$$\rho_{h_{l,pq}h_{l,p'q'}}(t, \Delta t) = \rho^{\mathrm{SB}_l}_{h_{l,pq}h_{l,p'q'}}(t, \Delta t) + \rho^{\mathrm{DB}_l}_{h_{l,pq}h_{l,p'q'}}(t, \Delta t). \tag{39}$$

Applying the corresponding distribution of LoS, ground reflection, and SB components, the STCF of the first tap can be expressed as follows

$$\rho^{\mathrm{LoS}}_{h_{1,pq}h_{1,p'q'}}(t,\Delta t)=\frac{K}{K+1}e^{-jk_0(A^{\mathrm{LoS}})}e^{j2\pi\Delta t(f_{\mathrm{Tm}}B^{\mathrm{LoS}}+f_{\mathrm{Rm}}C^{\mathrm{LoS}})} \tag{40}$$

with $A^{\mathrm{LoS}} = \Delta d_T[\cos(\alpha_T^{\mathrm{LoS}}-\alpha_T)\cos\beta_T^{\mathrm{LoS}}\cos\beta_T + \sin\beta_T^{\mathrm{LoS}}\sin\beta_T] + \Delta d_R[\cos(\alpha_R^{\mathrm{LoS}}-\alpha_R)\cos\beta_R^{\mathrm{LoS}}\cos\beta_R + \sin\beta_R^{\mathrm{LoS}}\sin\beta_R]$, $B^{\mathrm{LoS}} = \cos(\alpha_T^{\mathrm{LoS}}-\gamma_T)\cos\beta_T^{\mathrm{LoS}}\cos\xi_T + \sin\beta_T^{\mathrm{LoS}}\sin\xi_T$, and $C^{\mathrm{LoS}} = \cos(\alpha_R^{\mathrm{LoS}}-\gamma_R)\cos\beta_R^{\mathrm{LoS}}$, and

$$\rho^{\mathrm{Ref}}_{h_{1,pq}h_{1,p'q'}}(t,\Delta t)=\frac{\eta_r}{K+1}e^{-jk_0(A^{\mathrm{Ref}})}e^{j2\pi\Delta t(f_{\mathrm{Tm}}B^{\mathrm{Ref}}+f_{\mathrm{Rm}}C^{\mathrm{Ref}})} \tag{41}$$

with $A^{\mathrm{Ref}} = \Delta d_T[\cos(\alpha_T^{\mathrm{Ref}}-\alpha_T)\cos\beta_T^{\mathrm{Ref}}\cos\beta_T + \sin\beta_T^{\mathrm{Ref}}\sin\beta_T] + \Delta d_R[\cos(\alpha_R^{\mathrm{Ref}}-\alpha_R)\cos\beta_R^{\mathrm{Ref}}\cos\beta_R + \sin\beta_R^{\mathrm{Ref}}\sin\beta_R]$, $B^{\mathrm{Ref}} = \cos(\alpha_T^{\mathrm{Ref}}-\gamma_T)\cos\beta_T^{\mathrm{Ref}}\cos\xi_T + \sin\beta_T^{\mathrm{Ref}}\sin\xi_T$, and $C^{\mathrm{Ref}} = \cos(\alpha_R^{\mathrm{Ref}}-\gamma_R)\cos\beta_R^{\mathrm{Ref}}$. As for the SB scattering components in first tap, we have

$$\begin{aligned}\rho^{\mathrm{SB}_1}_{h_{1,pq}h_{1,p'q'}}(t,\Delta t) = \frac{\eta_{\mathrm{SB},1}}{K+1}\int_{-\pi}^{\pi}\int_{\beta_{1,1}}^{\beta_{1,2}}[e^{-jk_0(A^{\mathrm{SB}_1})} \\ \times e^{j2\pi\Delta t(f_{\mathrm{Tm}}B^{\mathrm{SB}_1}+f_{\mathrm{Rm}}C^{\mathrm{SB}_1})}] \\ \times f(\alpha_R^{\mathrm{SB}_1},\beta_R^{\mathrm{SB}_1})d(\alpha_R^{\mathrm{SB}_1},\beta_R^{\mathrm{SB}_1})\end{aligned} \tag{42}$$

with$A^{\mathrm{SB}_1} = \Delta d_T[\cos(\alpha_T^{\mathrm{SB}_1}-\alpha_T)\cos\beta_T^{\mathrm{SB}_1}\cos\beta_T + \sin\beta_T^{\mathrm{SB}_1}\sin\beta_T] + \Delta d_R[\cos(\alpha_R^{\mathrm{SB}_1}-\alpha_R)\cos\beta_R^{\mathrm{SB}_1}\cos\beta_R + \sin\beta_R^{\mathrm{SB}_1}\sin\beta_R]$, $B^{\mathrm{SB}_1} = \cos(\alpha_T^{\mathrm{SB}_1}-\gamma_T)\cos\beta_T^{\mathrm{SB}_1}\cos\xi_T + \sin\beta_T^{\mathrm{Ref}}\sin\xi_T$, and $C^{\mathrm{SB}_1} = \cos(\alpha_R^{\mathrm{SB}_1}-\gamma_R)\cos\beta_R^{\mathrm{SB}_1}$. Besides, for the other taps containing scattering components, we have

$$\begin{aligned}\rho^{\mathrm{SB}_l}_{h_{l,pq}h_{l,p'q'}}(t,\Delta t) = \eta_{\mathrm{SB},l}\int_{-\pi}^{\pi}\int_{\beta_{l,1}}^{\beta_{l,2}}[e^{-jk_0(A^{\mathrm{SB}_l})} \\ \times e^{j2\pi\Delta t(f_{\mathrm{Tm}}B^{\mathrm{SB}_l}+f_{\mathrm{Rm}}C^{\mathrm{SB}_l})}] \\ \times f(\alpha_R^{\mathrm{SB}_l},\beta_R^{\mathrm{SB}_l})d(\alpha_R^{\mathrm{SB}_l},\beta_R^{\mathrm{SB}_l})\end{aligned} \tag{43}$$

where $A^{SB_l} = \Delta d_T[\cos(\alpha_T^{\mathrm{SB}_l}-\alpha_T)\cos\beta_T^{\mathrm{SB}_l}\cos\beta_T + \sin\beta_T^{\mathrm{SB}_l}\sin\beta_T] + \Delta d_R[\cos(\alpha_R^{\mathrm{SB}_1}-\alpha_R)\cos\beta_R^{\mathrm{SB}_1}\cos\beta_R + \sin\beta_R^{\mathrm{SB}_1}\sin\beta_R]$, $B^{\mathrm{SB}_l} = \cos(\alpha_T^{\mathrm{SB}_l}-\gamma_T)\cos\beta_T^{\mathrm{SB}_l}\cos\xi_T + \sin\beta_T^{\mathrm{SB}_l}\sin\xi_T$, and $C^{\mathrm{SB}_l} = \cos(\alpha_R^{\mathrm{SB}_l}-\gamma_R)\cos\beta_R^{\mathrm{SB}_l}$, and

$$\begin{aligned}&\rho^{\mathrm{DB}_l}_{h_{l,pq}h_{l,p'q'}}(t,\Delta t) \\ &= \eta_{\mathrm{DB},l}\int_{-\pi}^{\pi}\int_{\beta_{1,1}}^{\beta_{1,2}}\int_{-\pi}^{\pi}\int_{\beta_{l,1}}^{\beta_{l,2}}[e^{-jk_0(A^{\mathrm{DB}_l})}e^{j2\pi\Delta t(f_{\mathrm{Tm}}B^{\mathrm{DB}_l}+f_{\mathrm{Rm}}C^{\mathrm{DB}_l})}] \\ &\times f(\alpha_R^{\mathrm{DB}_l},\beta_R^{\mathrm{DB}_l})f(\alpha_T^{\mathrm{DB}_l},\beta_T^{\mathrm{DB}_l}) \\ &\times d(\alpha_R^{\mathrm{DB}_l},\beta_R^{\mathrm{DB}_l})d(\alpha_T^{\mathrm{DB}_l},\beta_T^{\mathrm{DB}_l})\end{aligned} \tag{44}$$

where $A^{\mathrm{DB}_l} = \Delta d_T[\cos(\alpha_T^{\mathrm{DB}_l}-\alpha_T)\cos\beta_T^{\mathrm{DB}_l}\cos\beta_T + \sin\beta_T^{\mathrm{DB}_l}\sin\beta_T] + \Delta d_R[\cos(\alpha_T^{\mathrm{DB}_l}-\alpha_T)\cos\beta_T^{\mathrm{DB}_l}\cos\beta_T + \sin\beta_T^{\mathrm{DB}_l}\sin\beta_T]$, $B^{\mathrm{DB}_l} = \cos(\alpha_T^{\mathrm{DB}_l}-\gamma_T)\cos\beta_T^{\mathrm{DB}_l}\cos\xi_T + \sin\beta_T^{\mathrm{DB}_l}\sin\xi_T$, and $C^{\mathrm{DB}_l} = \cos(\alpha_R^{\mathrm{DB}_l}-\gamma_R)\cos\beta_R^{\mathrm{DB}_l}$.

B. DOPPLER PSD

The Doppler PSDs of the proposed channel model can be calculated by applying Fourier transform to local STCF with respect to time interval Δt, and the total Doppler PSD can be obtained by summing Doppler PSDs of every tap as

$$S_{h_{pq}h_{p'q'}}(f_D,t)=\sum_{l=1}^{L(t)}P_l(t)S_{h_{l,pq}h_{l,p'q'}}(f_D,t) \tag{45}$$

where f_D is the Doppler frequency that $|f_D| < f_{\mathrm{Rm}}+f_{\mathrm{Tm}}$, and Doppler PSD for each tap can be calculated as

$$S_{h_{l,pq}h_{l,p'q'}}(f_D,t)=\int_{-\infty}^{\infty}\rho_{h_{l,pq}h_{l,p'q'}}(t,\Delta t)e^{-j2\pi f_D\Delta t}d\Delta t. \tag{46}$$

C. RMS DELAY SPREAD

RMS-DS is one of the most important measures of wideband delay dispersion and can be calculated as the square root of the second central moment of the channel PDP [39], i.e.,

$$\sigma_\tau=\sqrt{\overline{\tau^2}-\overline{\tau}^2} \tag{47}$$

where

$$\overline{\tau^2}=\frac{\sum_{l=1}^{L(t)}P_l(t)\tau_l^2}{\sum_{l=1}^{L(t)}P_l(t)},\quad \overline{\tau}=\frac{\sum_{l=1}^{L(t)}P_l(t)\tau_l}{\sum_{l=1}^{L(t)}P_l(t)}. \tag{48}$$

D. TIME-VARIANT TRANSFER FUNCTION

The time-variant transfer function of proposed wideband model is defined as the Fourier transform of time-variant CIR $h_{pq}(t,\tau)$ with respect to time delay τ

$$H_{pq}(f,t)=\int_{-\infty}^{\infty}h_{pq}(t,\tau)e^{-j2\pi f\tau}d\tau. \tag{49}$$

Since the time delays are discrete in our model, the integral operation can be replaced by summation operation and time-variant transfer function can be expressed by

$$H_{pq}(f,t)=\sum_{l=1}^{L(t)}h_{l,pq}(t)e^{-j2\pi f\tau_l(t)}. \tag{50}$$

E. STATIONARY INTERVAL

The stationary interval is defined as the maximum duration during which WSS assumption is valid. Here, method of local region of stationary (LRS) is used to calculate the stationary

interval [40]. Firstly, the average PDP is obtained by taking average of N_{PDP} PDPs as

$$\overline{P}_h(t_k, \tau) = \frac{1}{N_{\mathrm{PDP}}} \sum_{k}^{k+N_{\mathrm{PDP}}-1} \left|h_{pq}(t_k, \tau)\right|^2. \tag{51}$$

The average time is chosen as $N_{\mathrm{PDP}} = 10$. Then the correlation coefficient between two APDPs in t_k and $t_k + \Delta t$ is obtained by

$$c(t_k, \Delta t) = \frac{\int \overline{P_h}(t_k, \tau) \cdot \overline{P_h}(t_k + \Delta t, \tau) d\tau}{\max\{\int \overline{P_h}(t_k, \tau)^2 d\tau, \int \overline{P_h}(t_k + \Delta t, \tau)^2 d\tau\}}. \tag{52}$$

At last, the stationary interval can be calculated as the largest interval within which the correlation coefficient beyond a certain threshold c_{thresh}, i.e.,

$$T_s(t_k) = \max\{\Delta t | c(t_k, \Delta t) \geq c_{\mathrm{threshold}}\}. \tag{53}$$

IV. SIMULATION MODEL AND RESULT ANALYSIS

In this section, an SoS simulation model is developed based on the previous analytical model by applying finite rays number in each cluster. Besides, derived statistical characteristics are analyzed at different time instants and scenarios. Finally, simulation results are compared with some available UAV-to-ground channel measurement results to validate the utility of proposed channel model.

A. SOS SIMULATION MODEL FOR WIDEBAND A2G CHANNELS

In the previous derivation, we use the analytical model assuming infinite rays in each scatterers, and channel statistical characteristics can be obtained by integral computation of the AoAs and AoDs. However, integral computation cannot be realized in channel simulator design. Hence, in order to make our channel model more practical, a SoS simulation model is developed by replacing integral computation with summation computation. Since in the integral computation, variables of integration are AoAs and AoDs, discrete AoAs and AoDs are introduced in the SoS model and other parameters are identical to those of the analytical model.

To obtain discrete AoAs and AoDs following certain distribution, the method of equal volume (MEV) is applied. The main idea of this method is applying inverse function of integration to generate the set of $\{\alpha_i, \beta_i\}_{i=1}^{N_i}$ meet the condition as

$$\int_{-\pi}^{\alpha_i} \int_{-\pi}^{\beta_i} f(\alpha, \beta) d\alpha d\beta = \frac{i - \frac{1}{4}}{N_i}. \tag{54}$$

The detailed description of this method is shown in [34]. Based on the MEV and our proposed model, the corresponding channel characteristics of SoS simulation model can be obtained by applying the discrete angular parameters and summation computation in derivation of channel characteristics in analytical model. Because of the limitation of length, there is no more repetition.

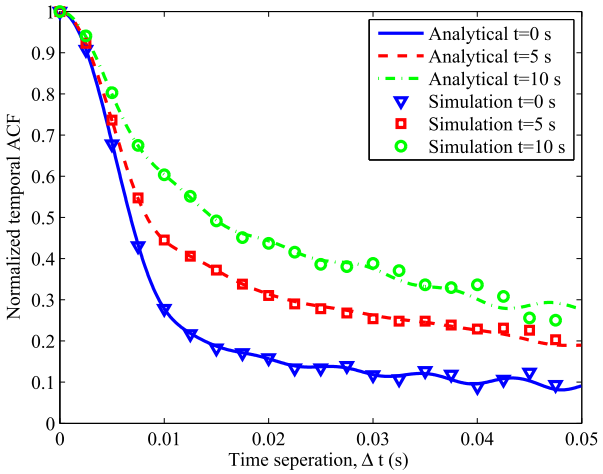

FIGURE 6. Analytical and simulation normalized temporal ACFs at different time instants ($f_c = 2.5$ GHz, $v_R = 3$ m/s, $v_T = 30$ m/s, $h_1 = 2$ m, $K = 0.3$, $L(t_0) = 10$, $\lambda_G = 0.8$, $\lambda_R = 0.08$).

B. CHANNEL CHARACTERISTICS ANALYSIS

In our simulation process, we consider a low-altitude UAV communication scenario, and the following parameters are chosen unless otherwise specified: $f_c = 2.5$ GHz, $D_{\mathrm{LoS}}(t = 0) = 1000$ m, $v_R = 3$ m/s, $v_T = 30$ m/s, $\gamma_T = \pi/4$, $\gamma_R = \pi/4$, $\xi_T = \pi/24$, $\alpha_T = \pi/12$, $\beta_T = \pi/6$, $\alpha_R = -\pi/3$, $\beta_R = -\pi/12$, $h_1 = 2$ m, $\alpha_\mu = \pi$, $k = 10$, $\varphi = \pi/24$, $L(t_0) = 10$, $\lambda_G = 0.8$, $\lambda_R = 0.08$. Note that in this paper, both movements of the UAV and ground terminal are taken into account. Considering that scatterers on the ground are mainly buildings, lamps, trees, etc., the heights of these scatterers are limited so the distant scattering EAoAs are set range from 0 to $\pi/12$. After repeatedly verification, the rays number in each scatterer is choosed as 50 in our SoS simulation model, which ensures both the accuracy and simplification.

Fig. 6 shows the temporal ACFs $\rho_{h_{pq}}(\Delta t)$ for analytical model and simulation model at different time instants. Temporal ACFs can be calculated as by setting $\Delta d_R = \Delta d_T = 0$ in (36). In different time instants, the temporal ACFs present shifting and the main reason is the changing of Doppler frequencies. It can also be seen that temporal ACFs of analytical model and simulation model match with each other at different time instants, which validates the correctness of the parameter generation method.

Fig. 7 presents the spatial CCFs $\rho_{h_{pq}h_{p'q}}(\Delta d_R)$ at Rx side for different time instants. Spatial CCFs can be calculated by setting $\Delta t = 0$ in (36). The variation of CCFs is due to the angular parameter shifting caused by movements of the UAV and ground terminal. Meanwhile, simulation results are compared with analytical results to ensures the correctness of our simulations and derivations.

Fig. 8 illustrates the Doppler PSDs of scattering components at different time instants. By analysis of Doppler PSD for scattering components in our simulation, it is observed that the Doppler PSD drift over time due to the movements

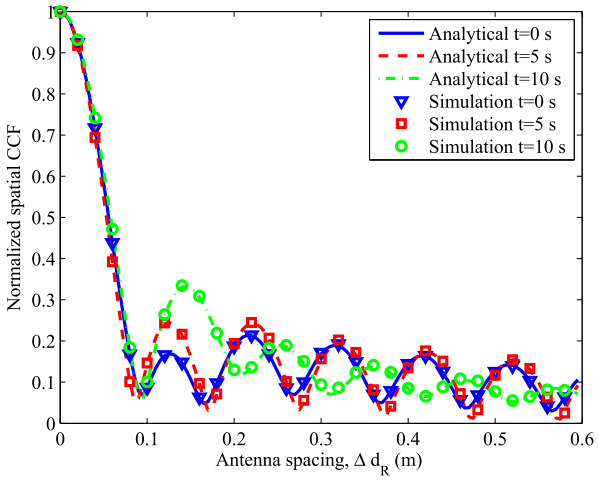

FIGURE 7. Analytical and simulation spatial CCFs at Tx side at different time instants ($f_c = 2.5$ GHz, $v_R = 3$ m/s, $v_T = 30$ m/s, $h_1 = 2$ m, $K = 0.3$, $L(t_0) = 10$, $\lambda_G = 0.8$, $\lambda_R = 0.08$).

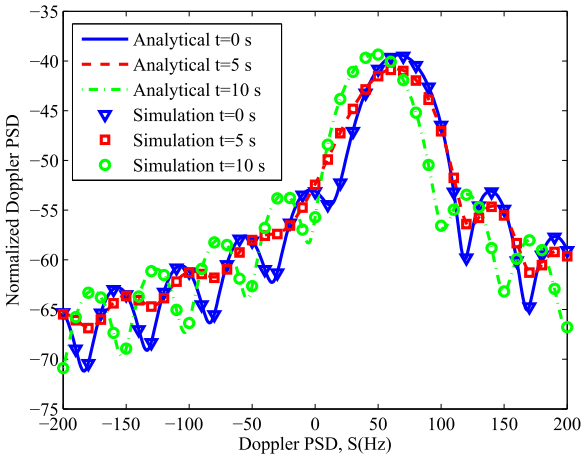

FIGURE 8. Analytical and simulation normalized Doppler PSDs at different time instants ($f_c = 2.5$ GHz, $v_R = 3$ m/s, $v_T = 30$ m/s, $h_1 = 2$ m, $K = 10$, $L(t_0) = 10$, $\lambda_G = 0.8$, $\lambda_R = 0.08$).

of UAV and ground terminal. Also the analytical results are compared with simulation results.

Fig. 9 presents the time-variant transfer functions of both non-stationary and WSS simulation model. In order to make proper comparison, we put both non-stationary and WSS transfer functions in colormap figures. We set the centre frequency to 2.5 GHz and band width to 10 MHz. At the beginning $t = 0$s, WSS model and non-stationary model have similar transfer function. As time goes on, transfer function of non-stationary model tends to have more frequent fluctuation. Therefore, our simulation model indeed presents more non-stationary channel properties of UAV-to-ground channels.

Fig. 10 compares the stationary interval in LoS and NLoS scenarios. In the NLoS scenario, the power of LoS and ground reflection components are set to zero, and the total power of scattering components are normalized to one. In the comparison results, the mean value of the stationary interval in LoS scenario is larger than that of the NLoS scenario.

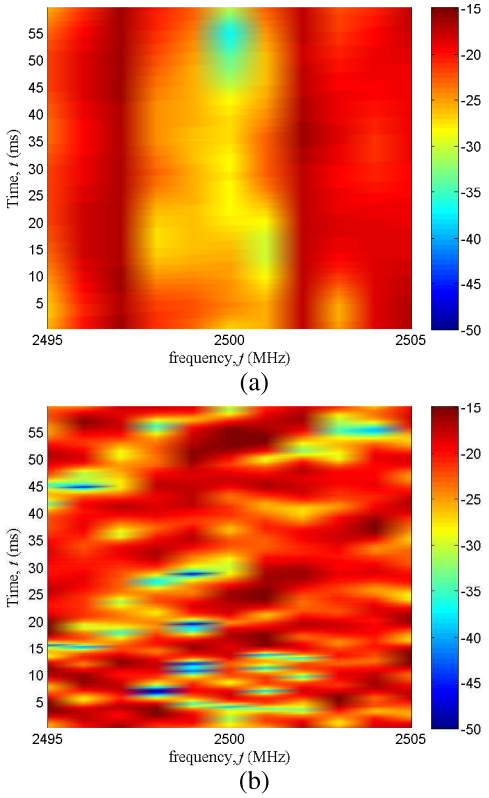

FIGURE 9. Time-variant transfer functions of WSS model and proposed non-stationary model ($f_c = 2.5$ GHz, $v_R = 3$ m/s, $v_T = 30$ m/s, $h_1 = 2$ m, $K = 0.3$, $L(t_0) = 10$, $\lambda_G = 0.8$, $\lambda_R = 0.08$).

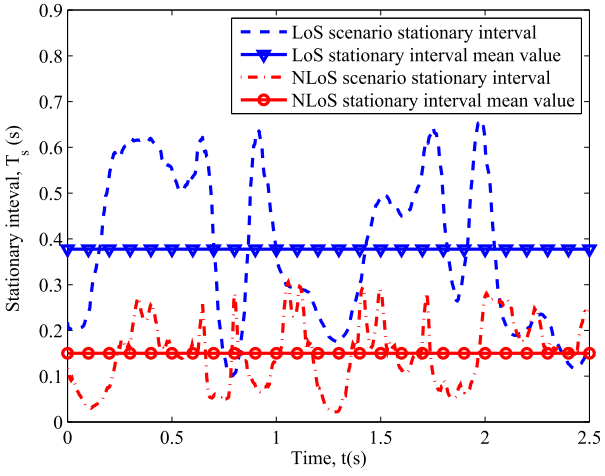

FIGURE 10. The stationary intervals with respect to time in LoS and NLoS scenarios ($f_c = 2.5$ GHz, $v_R = 3$ m/s, $v_T = 30$ m/s, $h_1 = 2$ m, $L(t_0) = 10$, $\lambda_G = 0.8$, $\lambda_R = 0.08$).

Besides, the stationary interval in NLoS scenario presents more frequent fluctuations than LoS scenario.

Fig. 11 gives the complementary cumulative distribution functions (CCDFs) of the stationary intervals with different UAV and ground terminal moving velocities. It can be observed that the higher moving velocities will reduce the periods of stationary intervals. The reason is that the higher velocities will lead to fast channel changing.

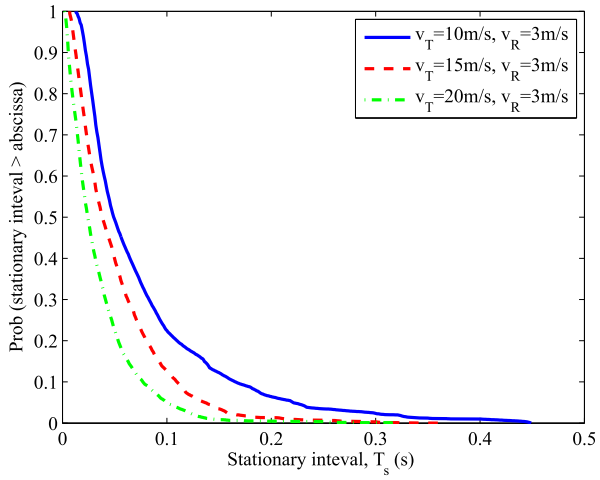

FIGURE 11. The CCDFs of stationary intervals with different UAV and ground terminal velocities for proposed model ($f_c = 2.5$ GHz, $v_R = 3$ m/s, $v_T = 30$ m/s, $h_1 = 2$ m, $L(t_0) = 10$, $K = 10$, $\lambda_G = 0.8$, $\lambda_R = 0.08$).

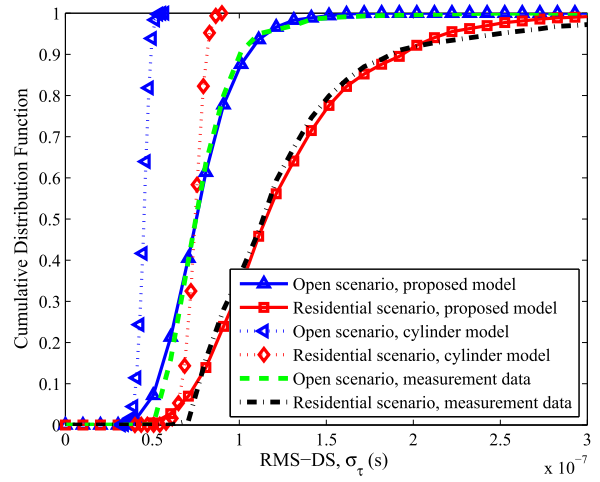

FIGURE 12. Comparison of RMS-DS with proposed model, cylinder model, and measurement data ($f_c = 2.5$ GHz, $v_R = 3$ m/s, $v_T = 30$ m/s, $h_1 = 2$ m, $L(t_0) = 10$, $\lambda_G = 0.8$, $\lambda_R = 0.08$, other parameters are in Table 2.

TABLE 2. Definition of simulation parameters.

	K	η_r	$\eta_{\mathrm{SB},l}$	r_τ	E$[\sigma]$	Std$[\sigma]$
Scenario 1	10.5	0.4	0.9	2.1	-6.2dB	0.49dB
Scenario 2	4.5	0.1	0.9	2.3	-6.5dB	0.52dB

C. MODEL VALIDATION

In order to verify the utility of our proposed model, we look for the A2G channel measurement results of RMS-DS, temporal ACF, and spatial CCF. Firstly, we give the fitting result of RMS-DS. The model validation simulation parameters are set according to measurement settings in [39]: $f_c = 2.5$ GHz, $D_{\mathrm{LoS}}(t = 0) = 500$ m, $h_1 = 2$ m, $\gamma_T = \pi$, $\gamma_R = \pi/4$, $\xi_T = 0$. The fitting parameters can be found in Table 2.

Fig. 12 compares the RMS-DS with proposed model, single cylinder model in [24], and measurement results at scenario 1 (open scenario) and scenario 2 (residential scenario).

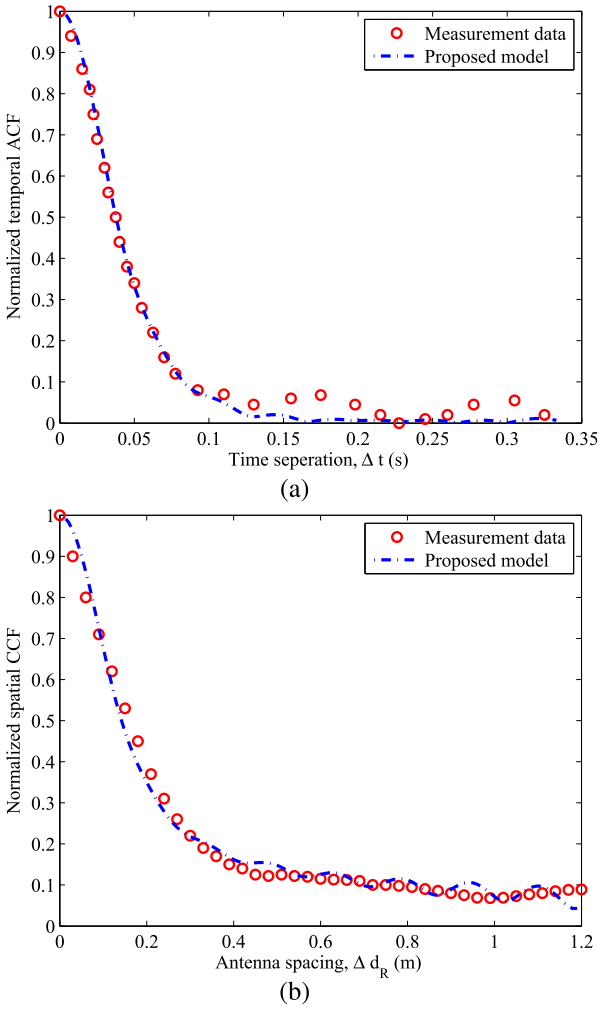

FIGURE 13. The comparsion of proposed GBSM and measurement results for (a) temporal ACFs and (b) spatial CCFs. (a) $f_c = 2.5$ GHz, $D_{\mathrm{LoS}}(t = 0) = 1000$ m, $v_R = 10$ m/s, $v_T = 40$ m/s, $\gamma_T = \pi$, $\gamma_R = \pi/4$, $\xi_T = 0$, $h_1 = 10$ m, $\varphi(t = 0) = \pi/3$. (b) $f_c = 2.6$ GHz, $D = 500$ m, $\gamma_T = \pi$, $\gamma_R = \pi/4$, $\xi_T = 0$, $h_1 = 10$ m, $\varphi(t = 0) = \pi/6$.

The single cylinder model also limited the scattering region to a certain height near the ground plane. It can be observed that proposed model has better fitting with measurement results compared with single cylinder model, which because that in our model different elliptical cylinder scattering regions are defined as different TDL structure with definable parameters. But for cylinder model, it's hard to define the scattering region at certain time delay.

Fig. 13 presents the comparison of temporal ACFs and spatial CCFs for measurement data and proposed simulation model. In Fig. 13(a), temporal ACF was obtained as flown distances divided by UAV velocity [35]. Theoretical temporal ACF was obtained from the proposed model with the parameters setting: $f_c = 2.5$ GHz, $D_{\mathrm{LoS}}(t = 0) = 1000$ m, $v_R = 10$ m/s, $v_T = 40$ m/s, $\gamma_T = \pi$, $\gamma_R = \pi/4$, $\xi_T = 0$, $h_1 = 10$ m, $\varphi(t = 0) = \pi/3$. In Fig. 13(b), we matched the simulation received spatial CCF with measurement data from [38]. The theoretical result of spatial CCF in Fig. 13(b) was obtained with simulation parameters as $f_c = 2.6$ GHz,

$D_{\mathrm{LoS}}(t = 0) = 500$ m, $\gamma_T = \pi$, $\gamma_R = \pi/4$, $\xi_T = 0$, $h_1 = 10$ m, $\varphi(t = 0) = \pi/6$. It can be found that the proposed simulation model also match well with measurement results.

V. CONCLUSIONS

In this paper, we have proposed a wideband non-stationary UAV-to-ground V2V GBSM, which is able to investigate the time-variant UAV-to-ground channels. Both movements of UAV and ground terminal have been taken into account. Besides, the cluster evolution process has been introduced to represent the scenario changing with respect to time. In order to make our model more accurate, the effective scattering region has been limited to near the ground plane and transition regions have been applied to provide a smooth cluster birth-death process. Based on the proposed model, some important channel characteristics have been derived, such as STCF, Doppler PSD, time-variant transfer function, RMS-DS, and stationary interval. The simulation results match the analytical results very well, showing the correctness of both derivations and parameter generation method. In addition, the RMS-DS, temporal ACF, and spatial CCF of the proposed channel models have been verified by measurements results, which confirms the correctness of our proposed model and simulation process. In the future, we plan to investigate the A2G channel model in millimeter wave band and evaluate UAV-aided communication performance based on our channel model.

APPENDIX
CALCULATION OF EFFECTIVE SCATTERING REGION

According to the property of the ellipsoid, the $l-$th tap delay scattering region having time delay τ_l correspond to scattering region which has the propagation distance $\tau_l c$ between $\mathbf{L}_T$, $\mathbf{S}_l$, and $\mathbf{L}_R$.

$$\| \mathbf{L}_T - \mathbf{S}_l \| + \| \mathbf{L}_R - \mathbf{S}_l \| = \tau_l c. \tag{55}$$

Substituting the expression of ground plane $z = 0$ into (55) and through further simplifying processing we can get effective scattering region on the ground plane

$$Ax^2 + By^2 + Cxy + Dx + Ey + F = 0 \tag{56}$$

where

$$\begin{aligned} A &= 4(c\tau_l)^2 - 4{y_T}^2 \\ B &= 4(c\tau_l)^2 - 4{x_T}^2 \\ C &= -8x_T y_T \\ D &= 4x_T H \\ E &= 4y_T H \\ F &= 4{z_R}^2(c\tau_l)^2 - H^2 \\ H &= c\tau_l + {x_T}^2 + {y_T}^2 + {z_T}^2 - {z_R}^2. \end{aligned}$$

In order to facilitate the calculation and expression, the ellipse general expression is used rather than the standard expression in [28].

REFERENCES

[1] T. Tomic, K. Schmid, P. Lutz, A. Domel, M. Kassecker, E. Mair, I. L. Grixa, F. Ruess, M. Suppa, and D. Burschka, "Toward a fully autonomous UAV: Research platform for indoor and outdoor urban search and rescue," *IEEE Robot. Autom. Mag.*, vol. 19, no. 3, pp. 46–56, Sep. 2012.
[2] *Project Loon*. Accessed: Feb. 18, 2015. [Online]. Available: https://www.google.com/loon
[3] *3GPP TR 36.777: Enhanced LTE Support for Aerial Vehicles*. Accessed: Jul. 13, 2017. [Online]. Available: https://www.3gpp.org/specs/archive/36_series/36.777
[4] X. Lin, V. Yajnanarayana, S. D. Muruganathan, S. Gao, H. Asplund, H.-L. Maattanen, M. B. A, S. Euler, and Y.-P. E. Wang, "The sky is not the limit: LTE for unmanned aerial vehicles," 2017, *arXiv:1707.07534*. [Online]. Available: https://arxiv.org/abs/1707.07534
[5] S. Hayat, E. Yanmaz, and R. Muzaffar, "Survey on unmanned aerial vehicle networks for civil applications: A communications viewpoint," *IEEE Commun. Surveys Tuts.*, vol. 18, no. 4, pp. 2624–2661, 4th Quart., 2016.
[6] Y. Zeng, R. Zhang, and T. J. Lim, "Wireless communications with unmanned aerial vehicles: Opportunities and challenges," *IEEE Commun. Mag.*, vol. 54, no. 5, pp. 36–42, May 2016.
[7] Q. Zhu, Y. Yang, X. Chen, Y. Tan, Y. Fu, C.-X. Wang, and W. Li, "A novel 3D non-stationary vehicle-to-vehicle channel model and its spatial-temporal correlation properties," *IEEE Access*, vol. 6, pp. 43633–43643, 2018.
[8] J. Bian, C.-X. Wang, J. Huang, Y. Liu, J. Sun, M. Zhang, and H. Aggoune, "A 3D wideband non-stationary multi-mobility model for vehicle-to-vehicle MIMO channels," *IEEE Access*, vol. 7, no. 1, pp. 32562–32577, Dec. 2019.
[9] A. Ghazal, Y. Yuan, C.-X. Wang, Y. Zhang, Q. Yao, Y. Yuan, H. Zhou, and W. Duan, "A non-stationary IMT-advanced MIMO channel model for high-mobility wireless communication systems," *IEEE Trans. Wireless Commun.*, vol. 16, no. 4, pp. 2057–2068, Apr. 2017.
[10] Y. Liu, C.-X. Wang, J. Huang, J. Sun, and W. Zhang, "Novel 3-D non-stationary mmWave massive MIMO channel models for 5G high-speed train wireless communications," *IEEE Trans. Veh. Technol.*, vol. 68, no. 3, pp. 2077–2086, Mar. 2019.
[11] Y. Liu, C.-X. Wang, C. F. Lopez, G. Goussetis, Y. Yang, and G. K. Karagiannidis, "3D non-stationary wideband tunnel channel models for 5G high-speed train wireless communications," *IEEE Trans. Intell. Transp. Syst.*, to be published.
[12] Y. Liu, A. Ghazal, C.-X. Wang, X. Ge, Y. Yang, and Y. Zhang, "Channel measurements and models for high-speed train wireless communication systems in tunnel scenarios: A survey," *Sci. China Inf. Sci.*, vol. 60, no. 8, Oct. 2017, Art. no. 101301. doi: 10.1007/s11432-016-9014-3.
[13] Y. Liu, C.-X. Wang, C. Lopez, and X. Ge, "3D non-stationary wideband circular tunnel channel models for high-speed train wireless communication systems," *Sci. China Inf. Sci.*, vol. 60, no. 8, Aug. 2017, Art. no. 082304. doi: 10.1007/s11432-016-9004-4.
[14] C. X. Wang, A. Ghazal, B. Ai, P. Fan, and Y. Liu, "Channel measurements and models for high-speed train communication systems: A survey," *IEEE Commun. Surveys Tuts.*, vol. 18, no. 2, pp. 974–987, 2nd Quart., 2016.
[15] C.-X. Wang, J. Bian, J. Sun, W. Zhang, and M. Zhang, "A survey of 5G channel measurements and models," *IEEE Commun. Surveys Tuts.*, vol. 20, no. 4, pp. 3142–3168, 4th Quart., 2018.
[16] S. Wu, C.-X. Wang, E.-H. M. Aggoune, M. M. Alwakeel, and X. H. You, "A general 3-D non-stationary 5G wireless channel model," *IEEE Trans. Commun.*, vol. 66, no. 7, pp. 3065–3078, Jul. 2018.
[17] A. Al-Hourani and K. Gomez, "Modeling cellular-to-UAV path-loss for suburban environments," *IEEE Commun. Lett.*, vol. 7, no. 1, pp. 82–85, Feb. 2018.
[18] D. W. Matolak and R. Sun, "Unmanned aircraft systems: Air-ground channel characterization for future applications," *IEEE Veh. Technol. Mag.*, vol. 10, no. 2, pp. 79–85, Jun. 2015.
[19] E. Yanmaz, R. Kuschnig, and C. Bettstetter, "Channel measurements over 802.11a-based UAV-to-ground links," in *Proc. GLOBECOM*, Dec. 2011, pp. 5–10.
[20] K. Takizawa, T. Kagawa, S. Lin, F. Ono, H. Tsuji, and R. Miura, "C-band aircraft-to-ground (A2G) radio channel measurement for unmanned aircraft systems," in *Proc. WPMC*, Sydney, NSW, Australia, Sep. 2014, pp. 754–758.
[21] Q. Feng, J. McGeehan, E. K. Tameh, and A. R. Nix, "Path loss models for air-to-ground radio channels in urban environments," in *Proc. VTC*, Melbourne, VIC, Australia, May 2006, pp. 2901–2905.

[22] Z. Shi, P. Xia, Z. Gao, L. Huang, and C. Chen, "Modeling of wireless channel between UAV and vessel using the FDTD method," in *Proc. WiCOM*, Beijing, China, Sep. 2014, pp. 100–104.
[23] N. Goddemeier and C. Wietfeld, "Investigation of air-to-air channel characteristics and a UAV specific extension to the rice model," in *Proc. GLOBECOM*, San Diego, CA, USA, Dec. 2015, pp. 1–5.
[24] L. Zeng, X. Cheng, C.-X. Wang, and X. Yin, "A 3D geometry-based stochastic channel model for UAV-MIMO channels," in *Proc. WCNC*, San Francisco, CA, USA, Sep. 2017, pp. 1–5.
[25] Y. Li and X. Cheng, "New deterministic and statistical simulation models for non-isotropic UAV-MIMO channels," in *Proc. WCSP*, Nanjing, China, Oct. 2017, pp. 1–6.
[26] L. Zeng, X. Cheng, C. X. Wang, and X. Yin, "Second order statistics of non-isotropic UAV ricean fading channels," in *Proc. IEEE VTC-Fall*, Toronto, ON, Canada, Sep. 2017, pp. 1–5.
[27] W. G. Newhall and J. H. Reed, "A geometric air-to-ground radio channel model," in *Proc. MILCOM*, Sep. 2002, pp. 632–636.
[28] M. Wentz and M. Stojanovic, "A MIMO radio channel model for low-altitude air-to-ground communication systems," in *Proc. IEEE VTC*, Boston, MA, USA, Sep. 2015, pp. 1–6.
[29] H. Jiang, Z. Zhang, and G. Gui, "Three-dimensional non-stationary wideband geometry-based UAV channel model for A2G communication environments," *IEEE Access*, vol. 7, pp. 26116–26122, 2019.
[30] H. Chang, J. Bian, C.-X. Wang, Z. Bai, J. Sun, and X. Gao, "A 3D wideband geometry-based stochastic model for UAV air-to-ground channels," in *Proc. IEEE GLOBECOM*, Abu Dhabi, UAE, Dec. 2018, pp. 206–212.
[31] A. Shaw and K. Mohseni, "A fluid dynamic based coordination of a wireless sensor network of unmanned aerial vehicles: 3-D simulation and wireless communication characterization," *IEEE Sensors J.*, vol. 11, no. 3, pp. 722–736, Mar. 2011.
[32] E. Yanmaz, R. Kuschnig, and C. Bettstetter, "Achieving air-ground communications in 802.11 networks with three-dimensional aerial mobility," in *Proc. IEEE INFOCOM*, Turin, Italy, Apr. 2013, pp. 120–124.
[33] J. Bian, J. Sun, C.-X. Wang, R. Feng, J. Huang, Y. Yang, and M. Zhang, "A WINNER+ based 3-D non-stationary wideband MIMO channel model," *IEEE Trans. Wireless Commun.*, vol. 17, no. 3, pp. 1755–1767, Mar. 2018.
[34] Y. Yuan, C. X. Wang, X. Cheng, B. Ai, and D. I. Laurenson, "Novel 3D geometry-based stochastic models for non-isotropic MIMO vehicle-to-vehicle channels," *IEEE Trans. Wireless Commun.*, vol. 13, no. 1, pp. 298–309, Jan. 2014.
[35] M. Simunek, F. P. Fontán, and P. Pechac, "The UAV low elevation propagation channel in urban areas: Statistical analysis and time-series generator," *IEEE Trans. Antennas Propag.*, vol. 61, no. 7, pp. 3850–3858, Jul. 2013.
[36] T. J. Willink, C. C. Squires, G. W. K. Colman, and M. T. Muccio, "Measurement and characterization of low-altitude air-to-ground MIMO channels," *IEEE Trans. Veh. Technol.*, vol. 65, no. 4, pp. 2637–2648, Apr. 2016.
[37] H. Jiang, Z. Zhang, J. Dang, and L. Wu, "Analysis of semi-ellipsoid scattering channel models for vehicle-to-vehicle communication environments," in *Proc. IEEE VTC-Fall*, Sydney, NSW, Australia, Jun. 2017, pp. 1–6.
[38] S. Payami and F. Tufvesson, "Channel measurements and analysis for very large array systems at 2.6 GHz," in *Proc. EuCAP*, Prague, Czech Republic, Mar. 2012, pp. 433–437.
[39] R. M. Gutierrez, H. Yu, Y. Rong, and D. W. Bliss, "Time and frequency dispersion characteristics of the UAS wireless channel in residential and mountainous desert terrains," in *Proc. CCNC*, Las Vegas, NV, USA, Jan. 2017, pp. 516–521.
[40] B. Chen, Z. Zhong, and B. Ai, "Stationarity intervals of time-variant channel in high speed railway scenario," *China Commun.*, vol. 9, no. 8, pp. 64–70, Aug. 2012.

HENGTAI CHANG received the B.Sc. degree from the School of Information Science and Engineering, Shandong University, Qingdao, China, in 2016, where he is currently pursuing the Ph.D. degree.

His current research interests include UAV communications, channel measurements, wireless propagation channel modeling, and 5G channel modeling.

JI BIAN received the B.Sc. degree in electronic information science and technology from Shandong Normal University, Jinan, China, in 2010, and the M.Sc. degree in signal and information processing from the Nanjing University of Posts and Telecommunications, Nanjing, China, in 2013. He is currently pursuing the Ph.D. degree with the School of Information Science and Engineering, Shandong University, Qingdao, China.

His current research interests include channel measurements, wireless propagation channel characterization, and 5G channel modeling.

CHENG-XIANG WANG (S'01–M'05–SM'08–F'17) received the B.Sc. and M.Eng. degrees in communication and information systems from Shandong University, China, in 1997 and 2000, respectively, and the Ph.D. degree in wireless communications from Aalborg University, Denmark, in 2004.

He was a Research Assistant with the Hamburg University of Technology, Hamburg, Germany, from 2000 to 2001, a Visiting Researcher with Siemens AG Mobile Phones, Munich, Germany, in 2004, and a Research Fellow with the University of Agder, Grimstad, Norway, from 2001 to 2005. He has been with Heriot-Watt University, Edinburgh, U.K., since 2005, where he was promoted to a Professor, in 2011. In 2018, he joined Southeast University, China, as a Professor. He is also a part-time professor with the Purple Mountain Laboratories, Nanjing, China. He has authored three books, one book chapter, and more than 350 papers in refereed journals and conference proceedings, including 23 Highly Cited Papers. He has also delivered 17 Invited Keynote Speeches/Talks and seven Tutorials in international conferences. His current research interests include wireless channel measurements and modeling, (B)5G wireless communication networks, and applying artificial intelligence to wireless communication networks.

Dr. Wang is a Fellow of the IET, an IEEE Communications Society Distinguished Lecturer, in 2019 and 2020, and a Highly-Cited Researcher recognized by Clarivate Analytics, in 2017 and 2018. He is currently an Executive Editorial Committee Member of the IEEE TRANSACTIONS ON WIRELESS COMMUNICATIONS. He has served as an Editor for nine international journals, including the IEEE TRANSACTIONS ON WIRELESS COMMUNICATIONS, from 2007 to 2009, the IEEE TRANSACTIONS ON VEHICULAR TECHNOLOGY, from 2011 to 2017, and the IEEE TRANSACTIONS ON COMMUNICATIONS, from 2015 to 2017. He was a Guest Editor of the IEEE JOURNAL ON SELECTED AREAS IN COMMUNICATIONS, Special Issue on Vehicular Communications and Networks (Lead Guest Editor), Special Issue on Spectrum and Energy Efficient Design of Wireless Communication Networks, and Special Issue on Airborne Communication Networks. He was also a Guest Editor for the IEEE TRANSACTIONS ON BIG DATA, Special Issue on Wireless Big Data, and is a Guest Editor for the IEEE TRANSACTIONS ON COGNITIVE COMMUNICATIONS AND NETWORKING, Special Issue on Intelligent Resource Management for 5G and Beyond. He has served as a TPC Member, a TPC Chair, and a General Chair for more than 80 international conferences. He received ten Best Paper Awards from IEEE GLOBECOM 2010, IEEE ICCT 2011, ITST 2012, IEEE VTC 2013-Spring, IWCMC 2015, IWCMC 2016, IEEE/CIC ICCC 2016, WPMC 2016, and WOCC 2019.

ZHIQUAN BAI (M'07) received the M.Eng. degree in communication and information system from Shandong University, Jinan, China, in 2003, and the Ph.D. degree (Hons.) in communication engineering from Inha University, Incheon, South Korea, in 2007, under the Grant of Korean Government IT Scholarship. From 2007 to 2008, he was a Postdoctoral Researcher with Inha University. From 2015 to 2016, he was a Visiting Professor with The University of British Columbia at Kelowna, Canada. Since 2007, he has been an Associate Professor with the School of Information Science and Engineering, Shandong University, China. His current research interests include cooperative and MIMO systems, visible light communications, cognitive radio networks, resource allocation and optimization, and 5G wireless communications.

WENQI ZHOU received the B.Sc. degree from Shandong Architecture University, in 2001, and the M.Sc. degree in control science and engineering from Shandong University, in 2006. He has been with Shandong Huahan Electronics Co., Ltd., since 2013, where he engaged in the research of information security, wireless communications, and intelligent robots. His current research interests include wireless channel characterization and modeling.

EL-HADI M. AGGOUNE (M'83–SM'93) received the M.S. and Ph.D. degrees in electrical engineering from the University of Washington (UW), Seattle, WA, USA. He taught graduate and undergraduate courses in electrical engineering at many universities in the USA and abroad. He served at many academic ranks, including an Endowed Chair Professor. He is listed as an Inventor in two patents assigned to the Boeing Company, USA, and the Sensor Networks and Cellular Systems Research Center, University of Tabuk, Saudi Arabia. He is also a Professional Engineer registered in Washington. He is currently serving as a Professor and the Director of the SNCS Research Center, University of Tabuk. His research is referred to in many patents, including patents assigned to ABB, Switzerland, and EPRI, USA. He has authored many papers in IEEE and other journals and conferences. His research interests include wireless sensor networks, energy systems, and scientific visualization. He is serving on many technical committees for conferences worldwide and a Reviewer for many journals. One of his Laboratories received the Boeing Supplier Excellence Award.

He was the recipient of received the IEEE Professor of the Year Award, UW Branch.